

Superior Oxygen Electrocatalysis on RuSe_x Nanoparticles for Rechargeable Air Cathodes

Ji-Hoon Jang, Eunjik Lee, Penghao Xiao, Kyusung Park, In Young Kim, Graeme Henkelman, Seong-Ju Hwang, Young-Uk Kwon,* and John. B. Goodenough*

A one-step, facile supercritical-ethanol-fluid synthesis of Se-modified Ru nanoparticles nucleated on carbon defects is reported, and it is demonstrated that these nanoparticles provide, with >70% efficiency at 1 A g⁻¹, a highly active and reversible oxygen-reduction/oxygen-evolution reaction on an air cathode in a nonaqueous electrolyte. The Se modification not only prevents Ru oxidation during charge/discharge cycling, but also improves the catalytic activity by promoting Li₂O₂ versus Li₂O deposited on the Ru particles during discharge. A computational calculation with density functional theory supports the role of a larger electron transfer to the oxygen of Li₂O₂ adsorbed on a surface layer of RuSe_{2-δ} than on a surface layer of RuO₂, thereby shifting the more stable adsorbent from Li₂O to Li₂O₂.

1. Introduction

Modern society depends on the energy stored in fossil fuels, and it is now realized that there is an urgent need to transition to other sustainable energy sources. This transition depends on our ability to store electrical energy generated by these alternative energy sources. The rechargeable battery offers a store that can be portable as well as stationary and dispersed. The voltage of a stable rechargeable battery with an aqueous electrolyte is restricted to about 1.5 V; batteries with an organic electrolyte have allowed realization of voltages of about 4 V, thus increasing the volumetric and specific energy densities that power the wireless revolution. Realization of a rechargeable

battery using oxygen as the cathode and a nonaqueous electrolyte would provide a step in energy density that could offer a commercially competitive electric vehicle;^[1,2] but this realization requires (1) a cathode catalyst providing fast, reversible oxygen-reduction and oxygen-evolution reactions (ORR and OER) on, respectively, discharge and charge; (2) a reversible alkali-metal anode. Here, we address the problem of catalyzing the reversible ORR/OER in a nonaqueous electrolyte.

A catalyst for an air cathode is normally a nanoparticle (NP) on the surface of a porous, electron-conducting substrate that is impregnated by a liquid electrolyte; air or O₂ is bubbled through the liquid in the pores of the substrate. The ORR on discharge produces an insoluble Li₂O₂ or Li₂O product that must be transformed back to Li⁺ and O₂ in the OER on charge, and Li₂O₂ is more easily decomposed. However, the stability of the air cathode in an aprotic electrolyte has remained a problem. Thus, there have been many efforts to improve the cell performance and to understand the operating mechanism such as exploring suitable electrolytes,^[3–7] separators,^[8,9] and the role of electrocatalysts.^[10–14] To date, the best cell performance and durability for the ORR/OER in a nonaqueous electrolyte has been achieved by employing a TiC cathode in dimethyl sulfoxide.^[15] Here, we report a facile synthesis of RuSe_x NPs on carbon that provide, in glyme as electrolyte, an air cathode with a better efficiency, capacity, and cyclability. Since an earlier study has identified defects in the carbon support of the electrocatalyst to be active centers for a reaction between the carbon and the electrolyte,^[16] we have used conventional air-electrode materials, but have nucleated the electrocatalyst at the defects in the carbon substrate to block this source of cathode degradation.

Polarizations of the ORR and OER increase the charging voltage V_{ch} for the OER and decrease the discharge voltage V_{dis} for the ORR, thereby reducing the efficiency V_{dis}/V_{ch} of electrical energy storage with an air electrode. Byon and co-workers^[17] have shown that certain metallic and/or metal-oxide NPs are able to promote, in the ORR, formation of poorly crystallized Li₂O₂ as a smooth coating on the surface of the NPs with a reduced overpotential (polarization) while carbon black does not. Therefore, we assume that the formation of an amorphous or small-grained Li₂O₂ product of the ORR, which is preferred versus Li₂O, can be deposited onto the surface of a NP catalyst, and catalytic NPs offer the largest catalytic surface

Dr. J.-H. Jang, Dr. K. Park, Prof. J. B. Goodenough
Texas Material Institute and Materials Science and Engineering Program
The University of Texas at Austin
Austin, TX 78712, USA
E-mail: jgoodenough@mail.utexas.edu

Dr. E. Lee, Prof. Y.-U. Kwon
Department of Chemistry
Sungkyunkwan University
Suwon 440-746, Republic of Korea
E-mail: ywkwon@skku.edu

Dr. P. Xiao, Prof. G. Henkelman
Department of Chemistry and the Institute for Computational
and Engineering Sciences
The University of Texas at Austin
Austin, TX 78712, USA

Dr. I. Y. Kim, Prof. S.-J. Hwang
Department of Chemistry and Nano Sciences
Ewha Womans University
Seoul 120-750, Republic of Korea

DOI: 10.1002/aenm.201702037

area. In addition, a first-principles calculation by Ceder and co-workers^[18] of the reaction kinetics of the reversible release of Li⁺ to the electrolyte and O₂ to the atmosphere in the OER has concluded that Li⁺ release is faster than O₂ release, making the release of O₂ from the catalytic surface the rate-limiting step of the OER if the Li₂O₂ product of the ORR remains on the catalytic surface. Therefore, a NP that has an appropriate oxygen affinity for both the homogeneous formation and retention of Li₂O₂ product of the ORR and for the Li₂O₂ decomposition in the OER appears to be the key to a good ORR/OER electrocatalyst in a nonaqueous electrolyte. This analysis reduces the problem to choosing and tuning a NP surface that provides the appropriate oxygen affinity provided the problem of the carbon/electrolyte degradation reaction is eliminated.

Transition-metal chalcogenides, particularly RuSe_x, have emerged as a new class of electrocatalysts for the ORR in room-temperature fuel cells that can replace the Pt-based electrocatalysts. Despite their potential, few studies of the electrocatalytic application of RuSe_x NPs have been made because a difficult and costly synthesis has been used.^[19–22] We have prepared RuSe_x NPs with RuCl₃·xH₂O and SeO₂ under supercritical-fluid conditions. The supercritical-ethanol-fluid (SCEF) process is an extremely effective way to synthesize RuSe_x nanocrystals since further heat treatment to form well-crystallized RuSe_x NPs is not needed. In the O₂-rich environment of the catalyst of an air cathode, the surface of an Ru NP catalyst will be oxidized to RuO₂, but the partial oxidation of Ru of RuSe_x NP catalyst is expected and makes it less prone to form RuO₂. Therefore, the negative charge on the oxygen of an adsorbed Li_xO NP will be greater if the Li_xO is adsorbed on an RuSe_x surface than on an RuO₂ surface, which is shown in the Theory section to shift the more stable adsorbed product of the ORR from Li₂O on an Ru NP to Li₂O₂ on an RuSe_x NP. Moreover, in this preparation, the electrocatalyst is nucleated predominantly at the defects in the carbon substrate.

Previous calculation has shown that the electrons transferred from Ru to Se come primarily from the Ru 5s and 5p electrons

and much less from the 4d electrons, which allows the electron transfer to modify the relative stabilization of the Li₂O₂ and Li₂O products over a wide area around a surface Se of an RuSe_x NP,^[23] and Stolbov et al. have used an ab initio study to argue that the charge transfer from Ru to an adsorbent species is the result of a surface-charge redistribution rather than an Ru 4d band-structure change.^[24] The modification of the relative stabilities of different adsorbed products of the ORR by a NP coating provides an interesting route to the tuning of an electrocatalytic activity. Starting with this point of view, we have suspected that well-dispersed Se on the surface of RuSe_x NPs might provide an efficient electrocatalyst for the ORR/OER at the cathode of a rechargeable Li-air battery having a nonaqueous electrolyte. As a result, we have not only optimized a facile SCEF synthesis of RuSe_x NPs, but have also demonstrated that these NPs have a remarkably active and efficient (>70%) electrocatalytic activity as well as cyclic durability.

2. Results and Discussion

2.1. Structural and Chemical Characterization

RuSe_x NPs on a carbon substrate, RuSe_x/C, were synthesized by a one-pot SCEF process (see the Experimental Section). Given that RuSe_x can only be obtained at high temperature,^[21,25] the low-temperature (350 °C) synthesis reported here can only provide a surface modification of an Ru NP. An identically controlled SCEF synthesis of the Ru from RuCl₃·xH₂O without the SeO₂ precursor gave a yield of <20%. Furthermore, the SeO₂ alone without the Ru precursor was not reduced to Se by the SCEF process according to X-ray diffraction (XRD) of the product (Figure S1a, Supporting Information). These observations indicate that Ru–Se interaction provides an intermediate seed for the formation of the RuSe_x NPs by the SCEF process, as is shown schematically in Figure 1. Figure S1b (Supporting Information) exhibits yields of the SCEF with several molar

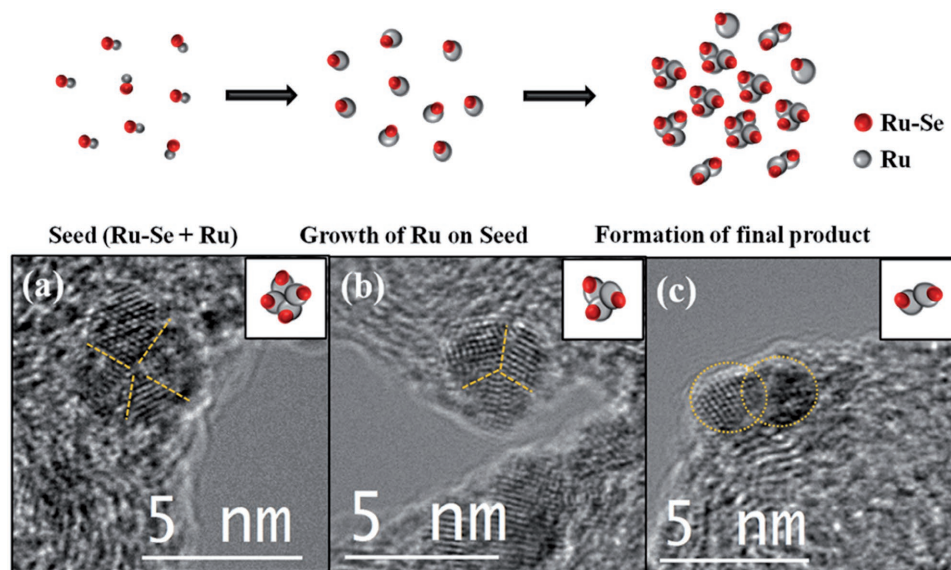


Figure 1. Top: Schematic illustration of the formation of RuSe_x NPs in the SCEF process. Bottom: High-magnification TEM images of RuSe_x NPs formed with a) 4 clusters, b) 3 clusters, and c) 2 clusters.

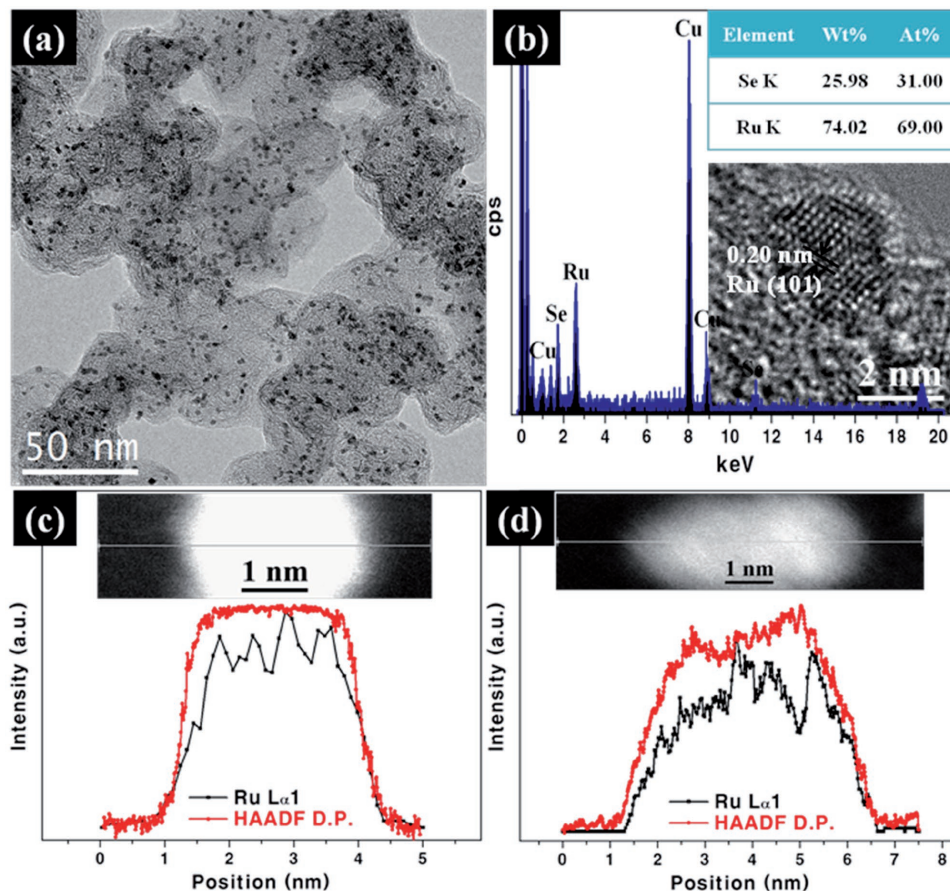


Figure 2. a) TEM images of RuSe_x NPs supported on KB carbon. b) EDS spectrum and quantitative analysis of an individual NP (marked in inset). EDS line profile of $\text{Ru L}\alpha 1$ overlapped with the NP's STEM-HAADF density profile for c) a 3.5 nm sized NP and d) two overlapped ≈ 3.0 nm sized NPs.

ratios of the Se/Ru precursors that were made for optimization of the SCEF process. For a comparative experiment, carbon-supported metallic Ru NPs (Ru/C) were prepared by ultrasound-assisted polyol synthesis (UPS).^[26,27] Carbon-supported Pt (Pt/C, 20 wt%) NPs, purchased from Premetek, were also used for a performance-comparison experiment.

Structural characterizations of the samples by XRD are shown in Figure S2 (Supporting Information) and by transmission electron microscopy (TEM) in Figure 1. The XRD peak at $2\theta = 25^\circ$ in Figure S2 (Supporting Information) corresponds to the (002) plane in the carbon support. A broad peak from RuSe_x at 43° in Figure S2a (Supporting Information) can be assigned to overlapping peaks at 38° , 42° , and 44° from Ru (100), (002), and (101) planes, respectively; the peaks at 59° , 69° , and 79° for high-indexed (102), (110), and (103) planes are consistent with those of the hexagonal-close-packed (hcp) structure of metallic Ru (JCPDS No. 06-0663). Other possible phases such as RuSe_2 , RuO_2 , SeO_3 , and SeO_2 were not detected in the full XRD spectrum, which indicates they were not present or exist only in amorphous form in the samples. The XRD spectrum for Ru/C was identical to that of RuSe_x/C , Figure S2b (Supporting Information). The high-resolution (HR) TEM images in Figure 1a–c reveal crystalline RuSe_x NPs consisting of 2, 3, or 4 micrograins with sharp boundaries between them, which supports our hypothesis of a seed and

growth formation of the RuSe_x NPs as shown schematically at the top of Figure 1.

Figure 2a shows a typical TEM image showing well-dispersed, uniformly sized RuSe_x NPs on the carbon substrate. Figure 2b shows an image of a typical individual NP; it is well crystallized with a 0.2 nm spacing between crystal planes corresponding to the spacing between (101) Ru planes. An elemental composition of $\text{Ru}/\text{Se} = 69.0/31.0$ in this particle is in good agreement with the Ru/Se ratio 68.8/31.2 obtained from inductively coupled plasma atomic emission spectroscopy (ICP-AES), Table S1 (Supporting Information). In contrast, RuSe_x NPs commonly prepared have poor crystallinity and require subsequent heating steps to obtain the crystallinity needed for the highest electrocatalytic activity, and this heating step results in particle growth. The RuSe_x NPs obtained by the one-step SCEF synthesis have good crystallinity and size uniformity. The average size of 250 NPs of Figure S3a,b (Supporting Information) is 2.6 ± 0.4 nm. In the same manner, we obtained an average size of 2.7 ± 0.3 nm for Ru NPs and 2.8 ± 0.5 nm for the Pt NPs as shown in Figure S3c–f (Supporting Information). Figure 2c shows an Ru EDS $\text{L}\alpha 1$ line profile of a single 3.5 nm RuSe_x NP taken on scanning from left to right across it along the gray line in the NP image with a 0.8 Å beam; a scanning transmission electron microscope-high angle annular dark field (STEM-HAADF) density profile is shown in the same plot.

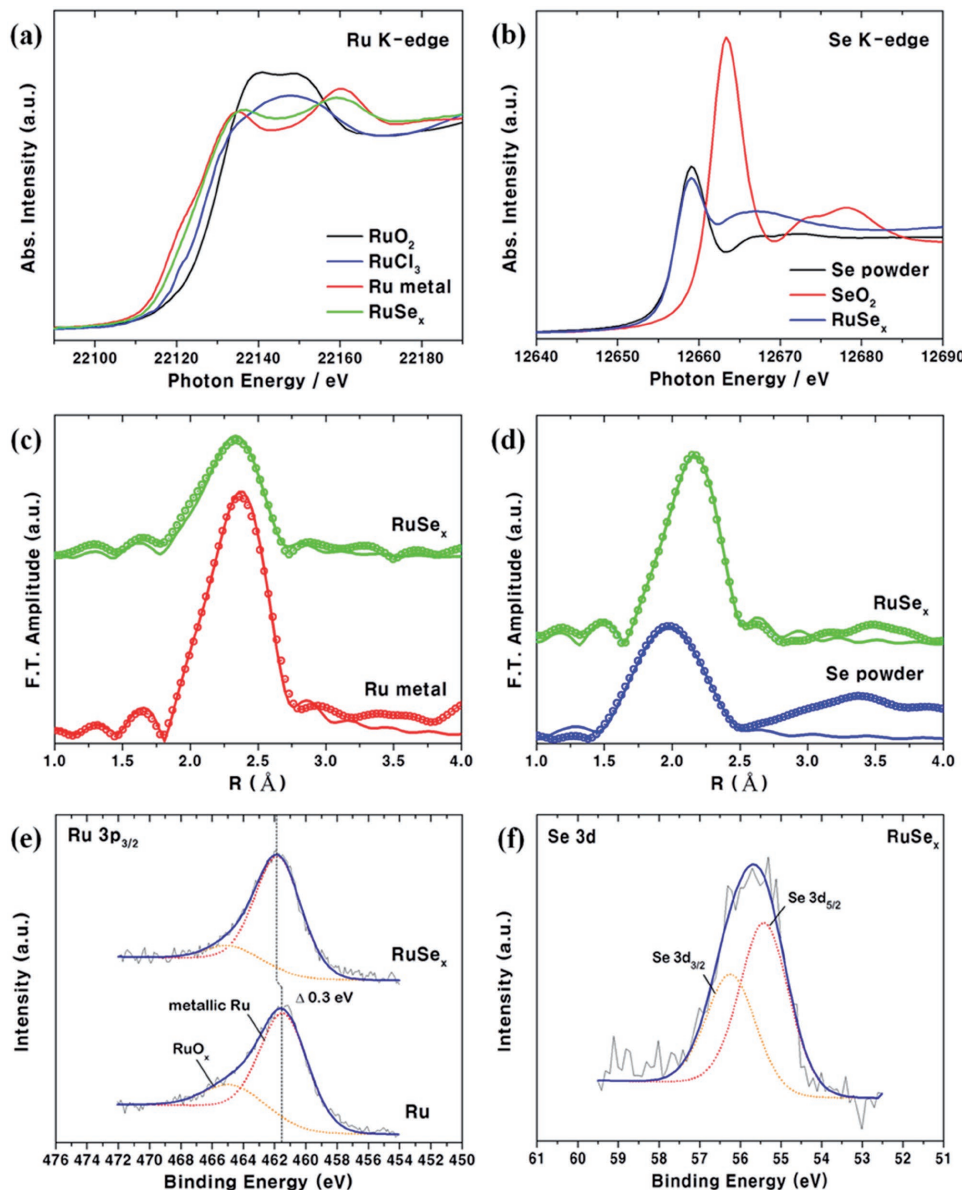


Figure 3. Comparison of the XANES spectral profiles for a) Ru-K edge of RuO₂ (black), RuCl₃ (blue), Ru metal (red), RuSe_x (green) and b) Se-K edge of Se powder (black), SeO₂ (red), RuSe_x (blue). c) Fourier-transformed radial distribution functions for Ru-K edge of Ru metal (Red), RuSe_x (green) and d) Se-K edge of Se powder (blue), RuSe_x (green). e) XP spectra for comparison of the Ru 3p_{3/2} BE in the Ru 3p_{3/2} RuSe_x and Ru in comparison with f) the Se 3d of RuSe_x.

The difference between the two scans shows clearly that the Se exists in a thin layer on the surface of an Ru NP. A similar conclusion is reached from the scans of Figure 2d across two smaller overlapping NPs.

Figure 3a,b shows X-ray absorption near-edge structure (XANES) at the Ru-K and Se-K edges at, respectively, 22 117 and 12 658 eV that were obtained to investigate the chemistries of the Ru and Se atoms in our RuSe_x NPs. The position of the Ru-K edge in the RuSe_x is slightly higher than that of Ru metal (Ru⁰) and lower than those of RuCl₃ (Ru³⁺) and RuO₂ (Ru⁴⁺), which indicates that the Ru is partially oxidized. The Se-K-edge spectrum of RuSe_x/C is close to that of Se powder, but with a reduced magnitude of the white line. This line is mainly caused

by a 1s to 4p electronic transition on the Se, and a partial filling of the 4p orbitals by Se reduction would reduce the magnitude of the line. At the Ru-K edge, Fourier-transformed-extended X-ray absorption fine structure (FT-EXAFS) spectra of RuSe_x/C showed the typical curve of hcp-Ru metal (Figure 3c). Compared with Ru metal, the decreased coordination number and distance of Ru–Ru is attributed to the decreased size of NPs and distortion by interaction with Se in Table S2 (Supporting Information). Zaikovskii et al. demonstrated that the Ru–Ru coordination number is decreased as the amount of Se increases.^[21] At the Se-K edge, FT-EXAFS spectra of RuSe_x/C showed that all Se atoms are bonded with Ru with low coordination number in Table S2 (Supporting Information).

In order to probe the electronic characteristics of the NPs, an X-ray photoelectron spectroscopy (XPS) analysis was carried out. Ru 3p_{3/2} XP spectra from RuSe_x/C and Ru/C samples were recorded with a monochromatic Al K α source. As shown in Figure 3e, the binding energy (BE) of the Ru 3p_{3/2} in RuSe_x/C is higher than that in the Ru/C sample by \approx 300 meV. Such a shift can be induced by a particle size effect or by electronic charge transfer. Since the sizes of both Ru and RuSe_x NPs are almost identical (Figure S3, Supporting Information), the phenomena should be ascribed to a charge transfer from Ru to Se, which corresponds well to the XANES results. Figure 3f shows the XP spectrum of Se for the RuSe_x/C recorded in the Se 3d region. Comparison of the Se 3d_{3/2} and 3d_{5/2} lines of selenium at 56.3 and 55.4 eV, respectively, with that of pure Se 3d_{5/2} at 55.6 eV shows no sign of either Se²⁻ (54.6 eV) or SeO₂ (59.2 eV) and demonstrates that there is only a little charge transfer between Ru and Se in the RuSe_x NPs.

2.2. Electrochemical Characterization

In order to investigate the electrochemical behavior of RuSe_x NPs in an air cathode, a prototype Swagelok cell was assembled in a typical cell configuration with glyme-based electrolyte. Carbonate-based electrolytes are decomposed under the measurement condition, resulting in the formation of byproducts such as Li₂CO₃, whereas glyme is known as a relatively stable electrolyte in the operation of a Li-air battery.^[4] For comparison, various cathode materials such as Ru/C, Pt/C, and carbon supports alone (Ketjen black 300J, KB) were assembled into identical cell configurations. We have focused particularly on the specific role of surface-charge redistribution on Ru by Se modification of the oxygen electrocatalysis; the reactivity of Ru/C electrocatalysis was compared directly to that of RuSe_x/C. First, we explored a cell in which the cathode was composed only of KB to clarify whether carbon black itself has an electrocatalytic role. As can be seen in Figure S4a (Supporting information), the carbon black cathode alone gives huge overpotentials for both the ORR (discharge) and OER (charge) as well as a cyclic instability. According to the recent report by Scrosati and co-workers,^[4] the glyme-based electrolyte can be easily decomposed by defects on a carbon surface during an electrochemical measurement. Because pristine KB is a porous carbon material containing a high fraction of dopant defects such as carbonyl groups, our result is in good agreement with the literature. Furthermore, a Pt/C electrocatalyst, which is commonly used in a cathode, shows an overpotential in the OER that is only slightly reduced from that with KB, which results in poor efficiency and durability of the cathode reactions. Figure S5 (Supporting Information) compares the first and second cycles of galvanostatic discharge/charge (GDC) measurements with RuSe_x and Ru NPs as catalysts; they were performed at 500 mA g⁻¹ cycle rate with a cutoff voltage of 2.6 and 4.0 V for discharge and charge, respectively. The ORR on both RuSe_x and Ru NPs occurred at \approx 2.7 V with a stable plateau and little capacity fade, but the specific capacities terminated at 2.6 V showed a huge difference, \approx 8800 mA h g⁻¹ for RuSe_x and \approx 5000 mA h g⁻¹ for the Ru-NP cathode. The difference in the catalytic performance is more marked in the OER. For the first

cycle, the RuSe_x NP cathode shows an onset potential of 3.3 V with the plateau region toward 3.7 V at 7200 mA h g⁻¹ whereas the Ru cathode gave higher onset (3.6 V) and plateau (3.9 V) potentials. The difference in the overpotential between those cathodes becomes larger in the second cycle. Clearly demonstrated is the improved reaction kinetics with the RuSe_x and Ru/C electrocatalysts, especially with the RuSe_x NPs, compared to cathodes of KB only. Furthermore, because the kinetics of the OER should be determined by the characteristics of the ORR product, we expected that the two NPs may have a different catalytic role for the discharge process.

Figure 4a displays the first GDC profiles of the cells comprised of RuSe_x/C cathodes measured at different current densities of 200, 400 and 800 mA g⁻¹. As expected, while the current-density variation does not affect the discharging profiles, the charging process shows a drastic distinction in overpotentials. At a current density of 200 mA g⁻¹ with a specific capacity of 2000 mA h g⁻¹, the RuSe_x NP cathode exhibits only \approx 700 mV potential difference for the ORR/OER reactions corresponding to $>$ 80% GDC efficiency. To confirm a cyclic durability of the cells at high current density, GDC profiles for RuSe_x/C and Ru/C were recorded at 1000 mA g⁻¹ over the limited specific capacity of 2000 mA h g⁻¹. In Figure 4b, Ru/C shows an initial cyclic efficiency of \approx 68% followed by a gradual increase of overpotential (or slow reaction kinetics) for both ORR and OER resulting in efficiency fading ($<$ 60%) after 50 cycles. On the other hand, Figure 4c indicates that the improved initial reaction kinetics with superior cycling efficiency $>$ 70% even after 100 cycles was obtained with an RuSe_x/C cathode. In addition, the GDC cycles of RuSe_x/C at 500 mA g⁻¹ limited by 2000 mA h g⁻¹ of specific capacity show \approx 80% initial GDC efficiency followed by only 5% efficiency decrease after 50 cycles (Figure S6, Supporting Information). Figure 4d summarizes the cell potentials at each ORR and OER step terminated by 2000 mA h g⁻¹, which reveals that RuSe_x/C has an excellent cycling performance compared to that of Ru/C.

Since both cycle life and kinetics are directly related to the formation/dissolution of discharge products of the ORR, we tried to analyze the cycled cathodes with HRTEM and XPS. Figure 5a,b shows TEM micrographs of RuSe_x/C after the 20th discharge and recharge cycles, respectively. Compared to the pristine RuSe_x/C particles shown in Figure 2a, the discharged RuSe_x/C shows a thin layer of oxide products coated along the surfaces of the electrocatalysts (Figure 5a); the layer is completely removed after the recharging process (Figure 5b). TEM micrographs of Ru/C after the 20th discharge and recharge cycles also show the formation and removal of thin oxide layer on the surface (Figure S7, Supporting Information).

The Li₂O₂ discharge product on RuSe_x/C was verified by Infrared (Figure S6, Supporting Information) and XPS (Figure 5d) analyses; however, due to their amorphous characteristic, the Li₂O₂ peaks were not detected in the XRD. In general, studies reported in the literature attribute a large overpotential in the OER to "toroidal" crystalline Li₂O₂ grown during discharging.^[17,28] These observations imply that RuSe_x/C electrocatalysts lead to the formation of amorphous Li₂O₂ with a uniform deposition that increases the reaction kinetics and reversibility. Figure 5c,d shows, respectively, the XP spectra of Ru/C and RuSe_x/C after the 50th GDC cycle. Even though

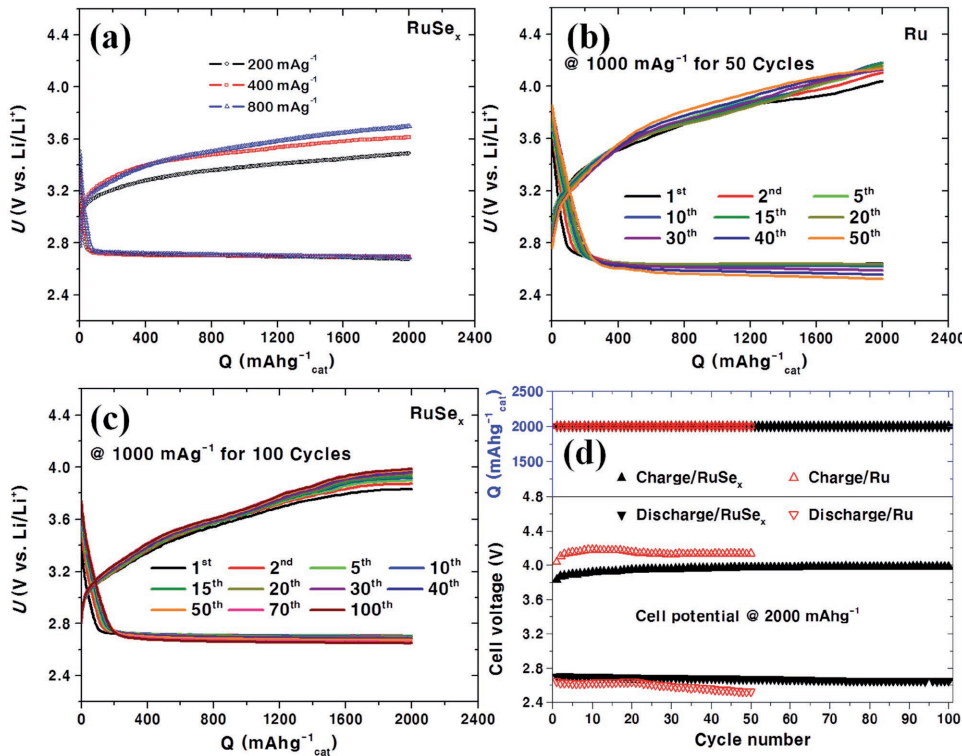


Figure 4. The voltage profiles of a) RuSe_x/C measured with different current densities of 200, 400, and 800 mA g⁻¹_{cat}; b,c) Ru/C for 50 cycles and RuSe_x/C for 100 cycles at a current of 1000 mA g⁻¹_{cat}, respectively. d) Comparison of the cycling performances of Ru/C and RuSe_x/C electrocatalysts. All data in this figure were recorded with a fixed specific capacity of 2000 mA h g⁻¹_{cat}.

many cycles were performed, all the components in both electrocatalysts are still retained without any chemical shift (Figures 5d; Figure S8a,b, Supporting Information). Note that while Li₂O₂ is repeatedly formed and decomposed during GDC cycles upon RuSe_x/C, the XPS and IR results (Figure S9, Supporting Information) show that a different Li₂O product is formed on the Ru/C NPs during discharge.

2.3. Theory

In order to elucidate the difference in discharged product formation on the RuSe_x/C and Ru/C NPs, we have employed density functional theory (DFT) calculations. First, the formation energies of bulk Li₂O₂ and Li₂O were calculated to set the baseline of further calculations

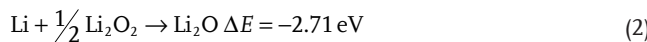
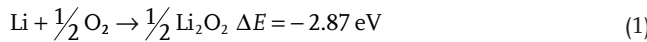


Figure 6a shows the convex hull of Li_xO_(1-x), where the formation energies are calculated as $E(\text{Li}_x\text{O}_{(1-x)}) = xE(\text{Li}) - \frac{1}{2}(1-x)E(\text{O}_2)$. Under equilibrium, any point above the hull will spontaneously decompose into the neighboring two points on the hull. The first observation that justifies our calculations is that both Li₂O₂ ($x = 1/2$) and Li₂O ($x = 2/3$) are on the hull. This means that the two phases can coexist under certain x

values, which agrees with many experimental observations.^[16] The open-circuit voltages form the Li₂O₂ and Li₂O compounds, which are proportional to the slopes between the points on the convex hull, are very close. From Equations (1) and (2), the voltage to form Li₂O₂ is higher by only 0.16 V. These voltage differences are in agreement with the 2.96 and 2.87 values from the experimental formation-energy data.^[29–31] The small voltage difference implies a possible mixing of the two product phases under a normal discharge.

It is well known that Ru metal binds oxygen too strongly to expose a metal surface to an oxygen-rich environment. To simplify, we assume that the active surfaces of the Ru NPs are fully oxidized by their O₂ exposure to the most stable RuO₂ (110) surface.^[32,33] The basin-hopping algorithm is employed to find the global formation-energy minima at different values of the product coverage; for a given coverage r in the range of $0.5 \leq r \leq 2$, the formation voltage of the most stable structure was calculated.^[34] Lowest-energy adsorbent structures for $r = 0.5$ and 1.0 are shown in Figure S10 (Supporting Information), and convex hulls of Li_xO_{1-x} on RuO₂ for different values of r are shown in Figure 6b. The average formation voltages for the Li₂O₂ and Li₂O products are also labeled in Figure 6b. The discharge voltage to form Li₂O₂ on a half-covered RuO₂ (110) surface changes little from that for the bulk case, Figure 6a, as also are the voltages for lithiating Li₂O₂ to Li₂O, and the Li₂O phase is the more stable on RuO₂.

Although the exact composition and structure of RuSe_x are unknown, we know that Se mixed with Ru is near the surface layers. With redundant Ru, all Se are negatively charged

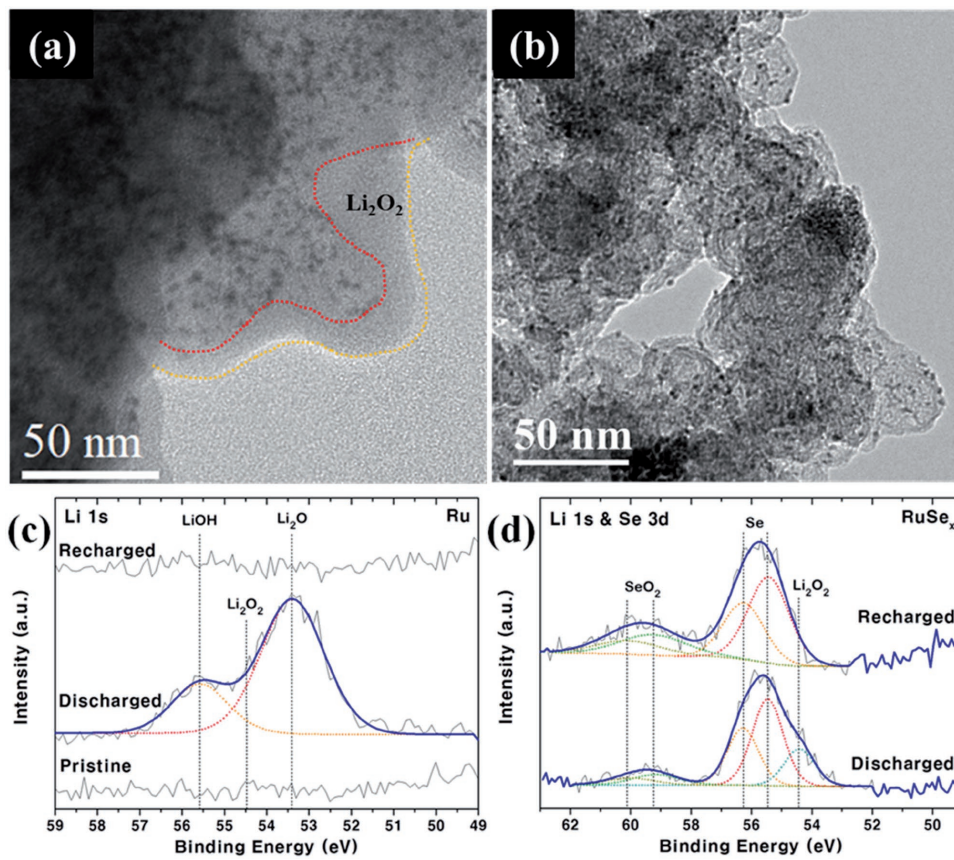


Figure 5. TEM micrographs of an RuSe_x/C cathode a) after 20 discharging cycles and b) recharging cycles. c) XP spectra for an Ru/C cathode after 50 GDC cycles and d) RuSe_x/C cathode after 50 GDC cycles.

and repel each other.^[35] Therefore, pyrite RuSe₂ (100) and (110) surfaces are used as simple models for comparison with the RuO₂. The convex hull in Figure 6c clearly shows RuSe₂ (100) stabilizes Li₂O₂ versus Li₂O, which thus moves the discharge

voltages of Equation (2) to lower values. As the product coverage grows from $r = 0.5$, the stabilization of the Li₂O₂ phase relative to the Li₂O becomes weaker, which may indicate the stabilization of the Li₂O₂ relative to the Li₂O phase is primarily

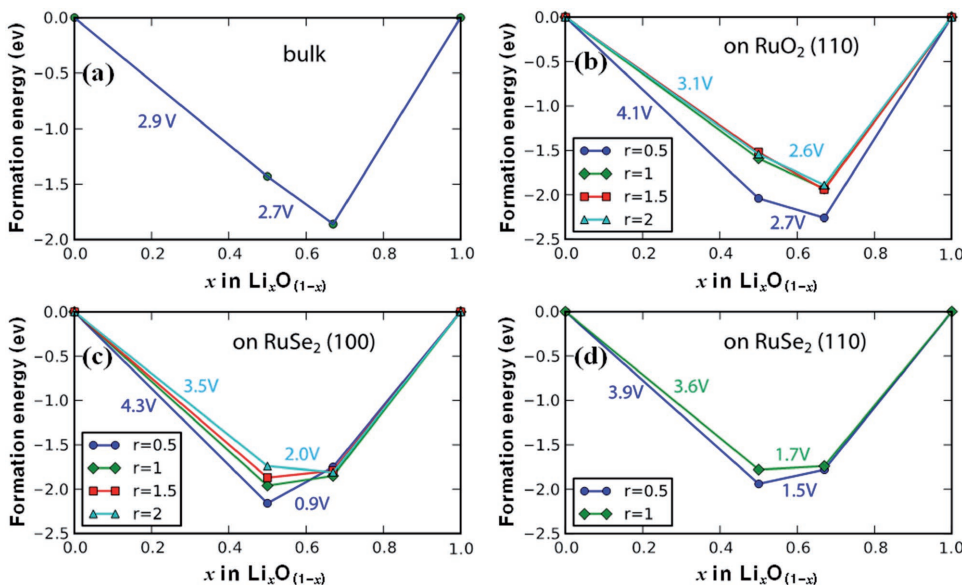


Figure 6. Convex hulls of a) $\text{Li}_x\text{O}_{(1-x)}$ as bulk, b) on RuO₂ (110), c) on RuSe₂ (100), and d) on RuSe₂ (110). Average voltages are labeled.

an electron transfer to the oxygen of Li_2O_2 from more Ru than those immediately neighboring the Li_2O_2 molecule rather than a strain energy associated with a lattice mismatch. Table S3 (Supporting Information) shows, from a Bader analysis,^[36,37] the negative charge on the oxygen of the Li_2O_2 adsorbed on RuO_2 is nearly the same as that of bulk Li_2O_2 whereas a significantly greater negative charge is on the oxygen of Li_2O_2 on RuSe_x . The more reduced Li_2O_2 on the RuSe_x NPs makes it more difficult to reduce the Li_2O_2 to Li_2O . On the other hand, the small differences in the negative charge on the oxygen of Li_2O_2 on RuO_2 compared to that of bulk Li_2O_2 results in the formation of a more stable Li_2O .

3. Conclusion

In summary, we have successfully developed a practical synthesis of crystalline NPs of RuSe_x/C by the SCEF method at 350 °C and shown that in glyme as the nonaqueous electrolyte, the RuSe_x NPs exhibit superior ORR/OER at an air cathode with >70% efficiency. Compared to pure Ru/C NPs, which form an RuO_2 surface layer on exposure to O_2 , the RuSe_x/C NPs exhibit a dramatic improvement in both the reaction kinetics and cyclic stability. Through a series of physical-chemistry characterizations, we have demonstrated that the Se is confined to an undefined surface $\text{RuSe}_{2-\delta}$ layer rather than to a monolayer of surface Se, and, according to TEM and XPS ex situ studies, the $\text{RuSe}_{2-\delta}$ surface layer stabilizes deposition of an amorphous Li_2O_2 rather than Li_2O product in the discharged ORR. A DFT calculation for Li_2O_2 and Li_2O products on RuO_2 shows that the Li_2O product is the more stable whereas on RuSe_{2-x} the Li_2O_2 product is the more stable.

4. Experimental Section

Synthesis of Electrocatalysts: RuSe_x/C was prepared by a facile one-pot SCFE process. To prepare the starting precursor solution, 0.4 mmol of $\text{RuCl}_3 \cdot x\text{H}_2\text{O}$ (Aldrich), 0.08 mmol of SeO_2 (Aldrich), and a certain amount of KB was added into a mixture of 16 mL of ethanol and oleylamine (50/50%, v/v). The solution was loaded in a 35 mL of Lab-made SCF reactor composed of tempered alloy steel, followed by heating in a Lab-made, shakable furnace at 623 K for 1 h. The final product was collected by several centrifuge removals of excess ethanol and completely dried in a vacuum oven at 353 K for 12 h.

Ru/C was prepared by a typical UPS method. Briefly, 0.1 mmol of Ruthenium acetylacetone (Aldrich, $\text{Ru}(\text{acac})_3$) and a certain amount of KB were added into an Ar prepurged ethylene glycol. The suspension was irradiated by ultrasound generated through a high-intensity ultrasonic probe (Sonic and Materials, VC-500, 30% amplitude, 20 kHz, 13 mm solid probe) for 3 h. During the synthesis, the reaction temperature was maintained constantly at 413 K by external heating. The dark slurry was then filtered with a membrane and washed/rinsed by ethanol, followed by drying in a vacuum desiccator at room temperature for 12 h.

Characterization: Powder diffraction patterns of all samples were recorded by XRD (DC/Max 2000, Rigaku, Cu $\text{K}\alpha$; $\lambda = 1.54056 \text{ \AA}$). XPS (Kratos Axis X-ray photoelectron spectrometer) measurements were performed with a monochromatic Al X-ray source (1486.6 eV). The spectra were calibrated in reference to graphitic carbon at 284.5 eV and fitted with the Gaussian–Lorentzian method with CasaXPS software. ICP-AES (Perkin Elmer) was used to determine the bulk compositions.

of the samples and the amount of loaded catalysts. The microstructure of the samples was observed with Cs-corrected HRTEM (Cs-HRTEM, JEOL JEM ARM 200F, 300 kV); energy-dispersive spectroscopy (EDS) recorded the elemental composition and microstructure of individual NPs in STEM mode. XANES spectra of the present materials were measured at Ru- and Se-K edge with the EXAFS facility installed at beam line 10C at the Pohang Accelerator Laboratory (PAL, Pohang, Korea, 2.5 GeV, and 180 mA). All the present data were collected in a transmission mode with gas-ionization detectors. The measurements were carried out at room temperature with a Si (111) single crystal monochromator. All the present spectra were carefully calibrated by measuring Ru or Se metal foil simultaneously. The data analysis for the experimental spectra was performed by the standard procedure reported previously.^[38]

Cell Fabrication: In cathode preparation, the carbon-supported electrocatalysts were thoroughly mixed with a polyvinylidene fluoride binder (PVDF) in *N*-methyl-2-pyrrolidone (NMP) solvent in a mass ratio of 88:12. The resulting slurries were coated onto a gas-diffusion media (Sigracet GDL 10BA) with a sample loading density of $\approx 0.6 \text{ mg cm}^{-2}$, followed by drying at 383 K for 12 h. As a controlled experiment, the cathode composed of only KB that used as carbon support was prepared by same procedure with a loading density of $\approx 0.5 \text{ mg cm}^{-2}$. A prototype Swagelok cell was assembled with a lithium-metal anode, glyme-based electrolyte (1 M LiCF_3SO_3 in tetraethylene glycol dimethyl ether (TEGDME)) immersed Celgard 2400 separator and a prepared cathode. The cathode preparation and sealing cells were carried out in an oxygen- and moisture-controlled Ar-filled glove box (both O_2 and H_2O level $< 0.1 \text{ ppm}$).

Electrochemical Studies: The electrochemical measurements were carried out with a LAND automatic battery cycler. In order to confirm a specific capacity for a specific potential range, the discharge–charge curves were recorded in the voltage range of 2.6–4.0 V at a constant current of 500 mA g⁻¹ for RuSe_x/C and Ru/C samples. The discharge–charge characteristics were verified by a constant specific capacity mode at several current densities. As controlled studies, KB only without any catalysts and Pt/C electrocatalysts were applied to the identical cell configuration described above. The recorded capacities were normalized by the total mass of electrocatalysts (electrocatalyst NPs + carbon supports).

Computational Details: All the calculations were performed with density functional theory in the Vienna ab initio Simulation Package (VASP). Core electrons were described by the projected augmented wave (PAW) method. A plane-wave basis set with an energy cut-off of 400 eV was employed. The exchange correlation energy was evaluated under the generalized gradient approximation (GGA) with the Perdew–Burke–Ernzerhof (PBE) functional.^[39–42] To reduce self-interaction error in the standard DFT, a Hubbard U term that penalizes fractional on-site occupancy was added to the Ru 4d orbitals.^[43] The effective U value ($U_{\text{eff}} = U - J$) was set to 2.5 eV.^[44,45]

Supporting Information

Supporting Information is available from the Wiley Online Library or from the author.

Acknowledgements

J.-H.J. and E.L. contributed equally to this work. This work was supported by the program “Materials and Interfacial Chemistry for Next Generation Electrical Energy Storage” funded by the U.S. Department of Energy (DESC0005397), Basic Science Research Program through the National Research Foundation of Korea (NRF) funded by the Ministry of Education (2009) and Welch Foundation (F-1841). The authors give special thanks to CCRF for TEM, NCIRF for ICP-AES, and TMI for XPS measurements.

Conflict of Interest

The authors declare no conflict of interest.

Keywords

electrocatalysts, Li-O₂ batteries, oxygen evolution reaction, oxygen reduction reaction, ruthenium selenide

Received: July 25, 2017

Revised: September 8, 2017

Published online: December 4, 2017

- [1] P. G. Bruce, S. A. Freunberger, L. J. Hardwick, J.-M. Tarascon, *Nat. Mater.* **2012**, *11*, 19.
- [2] Y.-C. Lu, B. M. Gallant, D. G. Kwabi, J. R. Harding, R. R. Mitchell, M. S. Whittingham, Y. Shao-Horn, *Energy Environ. Sci.* **2013**, *6*, 750.
- [3] D. Xu, Z.-L. Wang, J.-J. Xu, L.-L. Zhang, X.-B. Zhang, *Chem. Commun.* **2012**, *48*, 6948.
- [4] H.-G. Jung, J. Hassoun, J.-B. Park, Y.-K. Sun, B. Scrosati, *Nat. Chem.* **2012**, *4*, 579.
- [5] Y. Chen, S. A. Freunberger, Z. Peng, F. Bardé, P. G. Bruce, *J. Am. Chem. Soc.* **2012**, *134*, 7952.
- [6] B. Zhou, L. Guo, Y. Zhang, J. Wang, L. Ma, W.-H. Zhang, Z. Fu, Z. Peng, *Adv. Mater.* **2017**, *29*, 1701568.
- [7] S. Wu, J. Yi, K. Zhu, S. Bai, Y. Liu, Y. Qiao, M. Ishida, H. Zhou, *Adv. Energy Mater.* **2017**, *7*, 1601759.
- [8] J. L. Shui, J. S. Okasinski, D. Zhao, J. D. Almer, D. J. Liu, *ChemSusChem* **2012**, *5*, 2421.
- [9] S. H. Lee, J.-B. Park, H.-S. Lim, Y.-K. Sun, *Adv. Energy Mater.* **2017**, *7*, 1602417.
- [10] S. H. Oh, L. F. Nazar, *Adv. Energy Mater.* **2012**, *2*, 903.
- [11] Y.-C. Lu, H. A. Gasteiger, Y. Shao-Horn, *J. Am. Chem. Soc.* **2011**, *133*, 19048.
- [12] L. F. Li, D.-M. Tang, Y. Chen, D. Golberg, H. Kitaura, T. Zhang, A. Yamada, H. Zhou, *Nano Lett.* **2013**, *13*, 4702.
- [13] Z. Jian, P. Liu, F. Li, P. He, X. Guo, M. Chen, H. Zhou, *Angew. Chem., Int. Ed.* **2014**, *53*, 442.
- [14] P. Tan, M. Liu, Z. Shao, M. Ni, *Adv. Energy Mater.* **2017**, *7*, 1602674.
- [15] M. M. O. Thotiyil, S. A. Freunberger, Z. Peng, Y. Chen, Z. Liu, P. G. Bruce, *Nat. Mater.* **2013**, *12*, 1050.
- [16] J. Lu, Y. Lei, K. C. Lau, X. Luo, P. Du, J. Wen, R. S. Assary, U. Das, D. J. Miller, J. W. Elam, *Nat. Commun.* **2013**, *4*, 2383.
- [17] E. Yilmaz, C. Yogi, K. Yamanaka, T. Ohta, H. R. Byon, *Nano Lett.* **2013**, *13*, 4679.
- [18] Y. Mo, S. P. Ong, G. Ceder, *Phys. Rev. B* **2011**, *84*, 205446.
- [19] P. H. Camargo, Z. Peng, X. Lu, H. Yang, Y. Xia, *J. Mater. Chem.* **2009**, *19*, 1024.
- [20] G. Zehl, G. Schmithals, A. Hoell, S. Haas, C. Hartnig, I. Dorbandt, P. Bogdanoff, S. Fiechter, *Angew. Chem., Int. Ed.* **2007**, *46*, 7311.
- [21] V. I. Zaikovskii, K. S. Nagabushana, V. V. Kriventsov, K. N. Loponov, S. V. Cherepanova, R. I. Kwon, H. Bönnemann, D. I. Kochubey, E. R. Savinova, *J. Phys. Chem. B* **2006**, *110*, 6881.
- [22] H. Tellerm, A. Schechter, *J. Solid State Electrochem.* **2017**, <https://doi.org/10.1007/s1000801736161>.
- [23] S. Stolbov, *Phys. Rev. B* **2010**, *82*, 155463.
- [24] S. Stolbov, *J. Phys. Chem. C* **2012**, *116*, 7173.
- [25] M. J. F. Guinel, A. Bonakdarpour, B. Wang, P. K. Babu, F. Ernst, N. Ramaswamy, S. Mukerjee, A. Wieckowski, *ChemSusChem* **2009**, *2*, 658.
- [26] J.-H. Jang, E. Lee, J. Park, G. Kim, S. Hong, Y.-U. Kwon, *Sci. Rep.* **2013**, *3*, 2872.
- [27] J.-H. Jang, J. Kim, Y.-H. Lee, I. Y. Kim, M.-H. Park, C.-W. Yang, S.-J. Hwang, Y.-U. Kwon, *Energy Environ. Sci.* **2011**, *4*, 4947.
- [28] B. G. Kim, H.-J. Kim, S. Back, K. W. Nam, Y. Jung, Y.-K. Han, J. W. Choi, *Sci. Rep.* **2014**, *4*, 4225.
- [29] Y.-C. Lu, H. A. Gasteiger, M. C. Parent, V. Chiloyan, Y. Shao-Horn, *Electrochim. Solid-State Lett.* **2010**, *13*, A69.
- [30] F. Li, T. Zhang, H. Zhou, *Energy Environ. Sci.* **2013**, *6*, 1125.
- [31] M. W. Chase Jr., *J. Phys. Chem. Ref. Data, Monogr.* **1998**, *9*, 1506.
- [32] S. Shaikhutdinov, H.-J. Freund, *Annu. Rev. Phys. Chem.* **2012**, *63*, 619.
- [33] J. F. Weaver, *Chem. Rev.* **2013**, *113*, 4164.
- [34] D. J. Wales, J. P. Doye, *J. Phys. Chem. A* **1997**, *101*, 5111.
- [35] S. Zuluaga, S. Stolbov, *J. Phys.: Condens. Matter* **2012**, *24*, 345303.
- [36] R. F. W. Bader, *Atoms in Molecules: A Quantum Theory*, Oxford University Press, New York 1990.
- [37] W. Tang, E. Sanville, G. Henkelman, *J. Phys.: Condens. Matter* **2009**, *21*, 084204.
- [38] S.-J. Hwang, J.-H. Choy, *J. Phys. Chem. B* **2003**, *107*, 5791.
- [39] G. Kresse, J. Hafner, *Phys. Rev. B* **1993**, *47*, 558.
- [40] P. E. Blöchl, *Phys. Rev. B* **1994**, *50*, 17953.
- [41] G. Kresse, D. Joubert, *Phys. Rev. B* **1999**, *59*, 1758.
- [42] J. P. Perdew, K. Burke, M. Ernzerhof, *Phys. Rev. Lett.* **1996**, *77*, 3865.
- [43] S. Dudarev, G. Botton, S. Savrasov, C. Humphreys, A. Sutton, *Phys. Rev. B* **1998**, *57*, 1505.
- [44] H. Hadipour, M. Akhavan, *Eur. Phys. J. B* **2011**, *84*, 203.
- [45] P. Mahadevan, F. Aryasetiawan, A. Janotti, T. Sasaki, *Phys. Rev. B* **2009**, *80*, 035106.